

VAN-AD: Visual Masked Autoencoder with Normalizing Flow For Time Series Anomaly Detection

PengYu Chen, Shang Wan, Xiaohou Shi, Yuan Chang, Yan Sun, and Sajal K. Das, *Fellow, IEEE*

Abstract—Time series anomaly detection (TSAD) is essential for maintaining the reliability and security of IoT-enabled service systems. Existing methods require training one specific model for each dataset, which exhibits limited generalization capability across different target datasets, hindering anomaly detection performance in various scenarios with scarce training data. To address this limitation, foundation models have emerged as a promising direction. However, existing approaches either repurpose large language models (LLMs) or construct large-scale time series datasets to develop general anomaly detection foundation models, and still face challenges caused by severe cross-modal gaps or in-domain heterogeneity. In this paper, we investigate the applicability of large-scale vision models to TSAD. Specifically, we adapt a visual Masked Autoencoder (MAE) pretrained on ImageNet to the TSAD task. However, directly transferring MAE to TSAD introduces two key challenges: over-generalization and limited local perception. To address these challenges, we propose VAN-AD, a novel MAE-based framework for TSAD. To alleviate the over-generalization issue, we design an Adaptive Distribution Mapping Module (ADMM), which maps the reconstruction results before and after MAE into a unified statistical space to amplify discrepancies caused by abnormal patterns. To overcome the limitation of local perception, we further develop a Normalizing Flow Module (NFM), which combines MAE with normalizing flow to estimate the probability density of the current window under the global distribution. Extensive experiments on nine real-world datasets demonstrate that VAN-AD consistently outperforms existing state-of-the-art methods across multiple evaluation metrics. We make our code and datasets available at <https://github.com/PenyChen/VAN-AD>.

Index Terms—Time series anomaly detection, Vision foundation models, Masked autoencoders, Normalizing flow, IoT service systems.

I. INTRODUCTION

WITH the rapid development of Internet of Things (IoT) technologies and data acquisition techniques, time series analysis has attracted increasing attention, with major research tasks including forecasting [1], classification [2], and imputation [3]. Particularly, time series anomaly detection

(TSAD), which aims to identify abnormal patterns or observations in temporal data, has become a critical research problem because of its broad practical importance in intelligent service systems. In IoT-enabled service scenarios, TSAD can facilitate the real-time detection of device or sensor failures for proactive system maintenance and service continuity. Moreover, by analyzing the temporal behavior of connected devices in open environments, TSAD can help identify abnormal access, malicious operations, and other anomalous activities that may compromise the reliability and security of IoT services.

Deep learning methods have demonstrated impressive effectiveness in TSAD and have consequently received significant attention [4]–[6]. However, most existing methods still depend on dataset-specific model design and scenario-specific training. Although they often achieve competitive results in the environments for which they are developed, their ability to generalize across diverse target scenarios remains limited [7]. This lack of transferability poses a major obstacle to their practical adoption in IoT service systems, where training data are limited, annotation is expensive, and privacy or security constraints often prevent large-scale data sharing.

To address this challenge, recent studies have increasingly focused on developing foundation models for TSAD. According to the type of pre-training data, TSAD foundation models can be broadly categorized into TS-based and Text-based pre-training methods. TS-based methods rely on either collecting large-scale time series data from diverse domains or generating a wide variety of synthetic data. For instance, DADA [7] enhances the generalization capability of foundation models for anomaly detection by synthesizing anomalous samples. However, in real-world IoT service environments, anomalous time series are inherently sparse and difficult to obtain, making high quality large-scale pre-training datasets largely unavailable and thus constraining the development of TS-based methods. In contrast, Text-based methods seek to transfer the knowledge of large language models (LLMs), pretrained on massive text corpora, to TSAD tasks. For example, AnomalyLLM [8] employs GPT-2 as a teacher network and trains a student network via knowledge distillation, where anomalies are identified based on discrepancies between the outputs of the teacher and student networks. Nevertheless, the inherent modality gap between textual and temporal data raises concerns about the effectiveness of Text-based methods [9].

Recent studies have shown that pretrained vision models hold considerable potential for time series analysis. Compared with discrete textual data, both images and time series are

This work was supported by the National Natural Science Foundation of China under Grant 62272052. Yan Sun is the corresponding author.

Pengyu Chen, Shang Wan and Yan Sun are with the School of Computer Science (National Pilot Software Engineering School), Beijing University of Posts and Telecommunications, Beijing 100876, China (e-mail: penyuchen@bupt.edu.cn; 25110739@bupt.cn; sunyan@bupt.edu.cn).

Xiaohou Shi and Yuan Chang are engineers of China Telecom Research Institute Beijing, China (e-mail: shixh6@chinatelecom.cn; changy8@chinatelecom.cn).

Sajal K. Das is with the Department of Computer Science, Missouri University of Science and Technology, Rolla, MO 65409 USA (e-mail: sdas@mst.edu).

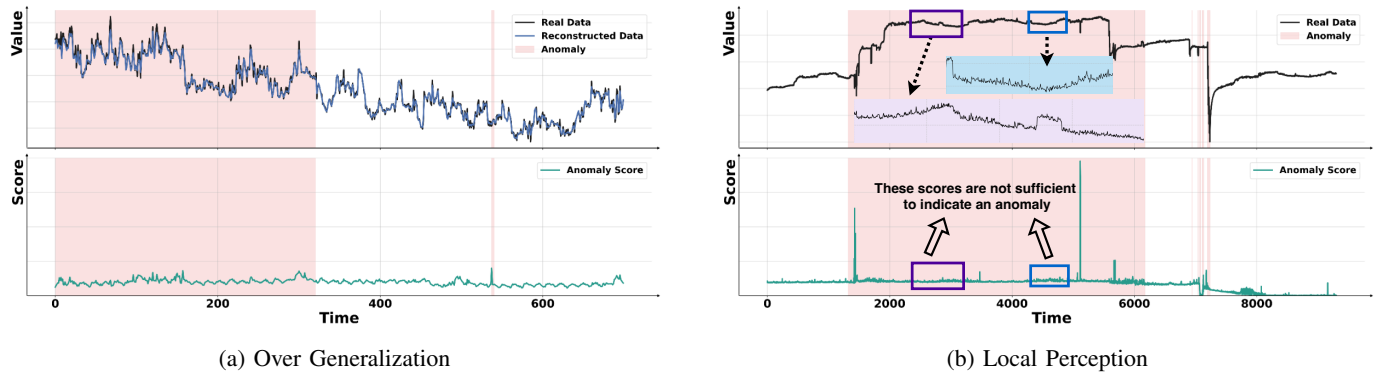


Fig. 1: Examples of the over-generalization and local-perception issues of MAE in TSAD on the PSM dataset. The red background indicates anomalous segments. Fig. 1a illustrates the over-generalization problem of MAE: both anomalous and normal sequences can be reconstructed well, resulting in similarly low anomaly scores. Fig. 1b illustrates the local-perception issue of MAE. When the current window is fully occupied by an anomalous segment, the variations within the window often fail to reflect abnormal behavior, leading to a low anomaly score.

inherently continuous, and images often exhibit structural characteristics that are also common in real-world temporal signals, such as trends, seasonality, and abrupt changes [10]–[12]. Such structural alignment suggests that vision models may provide a more suitable transfer source for time series tasks than Text-based models. For example, VisionTS [10] and VisionTS++ [11] achieve impressive zero-shot forecasting performance by converting time series segments into two-dimensional grayscale images and leveraging a Masked Autoencoder (MAE). Likewise, ViTST [12] validates the effectiveness of the Vision Transformer for time series classification through line-chart rendering. However, despite these encouraging results, the use of pretrained vision models for TSAD in practical environments remains at an early stage and has not yet been sufficiently investigated.

Inspired by VisionTS [10], we further explore the potential of the visual Masked Autoencoder (MAE) [13] for TSAD. Through pre-training on large-scale natural image datasets, MAE has learned rich continuous representations whose underlying structural patterns exhibit notable similarities to the temporal dynamics of time series, such as trends and seasonality. This observation suggests that natural images may provide transferable prior knowledge for modeling normal temporal regularities. Based on this intuition, we argue that a pretrained MAE can reconstruct normal sequences that follow regular temporal patterns more effectively than anomalous sequences that violate such regularities. Accordingly, the reconstruction error produced by the pretrained MAE can be used to assess the anomaly level of each time point.

However, directly transferring MAE to TSAD remains challenging. One key issue is the over-generalization problem caused by the strong reconstruction capability of MAE [14]. Specifically, MAE may reconstruct anomalous points nearly as well as normal ones, thereby reducing the reconstruction contrast between normal and abnormal patterns, as illustrated in Fig. 1a. A further limitation arises from the commonly used fixed sliding window scheme, which restricts the model’s ability to detect long anomalies. Due to the quadratic computational complexity of the Transformer [15], the window

length is usually constrained to a relatively small size (e.g., 100 or 196), preventing the model from capturing sufficient long context. As shown in Fig. 1b, when an entire window is occupied by an anomalous segment, the local temporal dynamics within that window may appear normal rather than abnormal. Without access to a broader temporal context, the model may reconstruct such a segment well and mistakenly interpret it as a normal temporal variation, thereby impairing anomaly detection performance.

To overcome these limitations, we propose **VAN-AD: Visual Masked Autoencoder with Normalizing Flow for Time Series Anomaly Detection**. To adapt MAE to TSAD, we first encode multivariate time series into a variable time heatmap matrix and introduce a checkerboard masking strategy to construct complementary image pairs, allowing the MAE to reconstruct masked regions from the visible ones. This masking mechanism encourages the model to capture both inter-variable dependencies and temporal correlations during reconstruction, thereby improving its ability to recover complex patterns.

To mitigate the over generalization issue, we further design an Adaptive Distribution Mapping Module (ADMM). We observe that, although MAE can reconstruct anomalous sequences, the reconstructed outputs are often smoother and exhibit less local variation than the original sequences. As a result, directly comparing the original and reconstructed sequences may underestimate their discrepancy, because they are not fully aligned in the same statistical space. To address this issue, ADMM incorporates the statistics of the original sequence and maps the reconstructed sequence back into that statistical space, so that discrepancies induced by abnormal patterns can be further amplified.

Finally, to overcome the limitation of local context perception, we introduce a Normalizing Flow Module (NFM). Specifically, NFM takes the output of MAE and further models the probability distribution of normal patterns. In this way, VAN-AD can not only exploit MAE to capture local reconstruction information, but also estimate the density of the current window with respect to the global distribution of normal patterns, thereby enabling more accurate anomaly

detection.

Our main contributions are summarized as follows:

- We propose VAN-AD, a novel framework that adapts pretrained MAE to time series anomaly detection. Different from existing TS-based and Text-based pretraining methods, VAN-AD explores vision-based transfer for TSAD.
- We design an Adaptive Distribution Mapping Module (ADMM) to alleviate the over generalization issue of MAE in TSAD, and introduce a Normalizing Flow Module (NFM) to model the global probability distribution of normal patterns, thereby compensating for the limited context perception of MAE.
- We conduct extensive experiments on nine real-world datasets. Experimental results show that VAN-AD consistently outperforms existing TS-based and Text-based pretraining methods, and other state-of-the-art baselines.

II. RELATED WORK

This section summarizes related work on time series anomaly detection and recent research on image-based time series analysis.

A. Time Series Anomaly Detection

Traditional TSAD methods can be classified into non-learning [16], [17] and machine learning [18], [19]. In recent years, deep learning methods have achieved remarkable success in time series anomaly detection. These methods can be broadly classified into three main categories: forecasting-based [20], reconstruction-based [4], [21], and contrastive-based approaches [22], [23]. Forecasting-based methods identify anomalies through prediction errors. For example, GDN [20], captures inter variable dependencies and uses deviations between predicted and observed values as anomaly signals. Reconstruction-based methods detect anomalies according to reconstruction error, under the assumption that normal patterns are easier to reconstruct than abnormal ones. Representative methods such as CATCH [4] and MTSCID [21] improve detection by jointly modeling temporal and frequency information. Contrastive-based methods focus on learning discriminative representations, where normal patterns are encouraged to cluster while anomalous patterns are separated. For instance, CAROTS [23] incorporates causal information into contrastive learning to enhance anomaly discrimination.

Although these methods achieve strong performance on specific datasets, they generally require dataset-specific training and therefore are difficult to transfer to new scenarios where data are scarce or privacy constraints are strict. As a result, foundation models for TSAD have recently attracted increasing attention. According to the modality of pre-training data, existing approaches can be broadly divided into TS-based and Text-based methods. Among TS-based based methods, DADA [7] constructs anomalous samples during pre-training through heuristic anomaly injection and explicitly improves the discriminability between normal and abnormal patterns via Adaptive Bottlenecks and Dual Adversarial Decoders. Other foundation models, such as Time-MoE [24], Chronos [25],

and Timer [26], are pretrained on diverse real-world time series datasets collected from multiple domains, and assess the anomaly level of each time point based on prediction errors.

Despite these advances, high quality pre-training datasets specifically designed for anomaly detection remain largely unavailable because anomalous patterns are inherently scarce. As a result, existing TS-based methods still face difficulties when dealing with complex evolution patterns commonly observed in industrial scenarios. Text-based methods provide an alternative direction. GPT4TS [27] adapts LLMs to TSAD through fine-tuning. AnomalyLLM [8], in contrast, uses GPT-2 as a teacher model to supervise a student network through knowledge distillation, and identifies anomalies according to the discrepancy between the teacher and student outputs. Zhang et al. [28] further explores the use of GPT-4 and Claude-2 for anomaly detection and requires the models to provide explanations for their decisions. Nevertheless, because LLMs are inherently developed for discrete textual data, whereas time series are continuous signals, the substantial modality gap makes it difficult for such methods to capture the underlying evolution patterns of time series. Consequently, the effectiveness of Text-based methods for TSAD has been increasingly questioned [9], [29].

B. Image-based Time Series Analysis

In recent years, Image-based methods have shown considerable potential in time series analysis. AST [30] employs DeiT [31] for time series classification, while ViTST [12] further explores this direction by leveraging pretrained Vision Transformers. VisionTS [10] demonstrates that the visual Masked Autoencoder exhibits remarkable zero-shot transferability in time series forecasting, and its follow-up work, VisionTS++ [11], further enhances the representational capacity of cross-modal foundation models through continued pretraining of the visual backbone. In addition, Ni et al. [32] systematically review the potential of vision models for time series analysis, highlighting that two-dimensional image representations can more naturally preserve the structural information of complex fluctuations. Zhao et al. [33] further provide a comprehensive evaluation of large-scale vision models for time series processing, confirming the strong inductive bias introduced by visual pretraining.

Despite these encouraging results in time series forecasting and classification, the application of vision models to TSAD remains at an early stage. In particular, the use of large-scale vision models for TSAD is still largely underexplored. Existing studies have not yet provided effective designs for adapting vision foundation models to anomaly detection, leaving substantial room for investigating an anomaly detection framework based on vision models.

III. PRELIMINARIES

This section first introduces the concept of time series anomaly detection, and then summarizes the definition of visual masked autoencoders and normalizing flow.

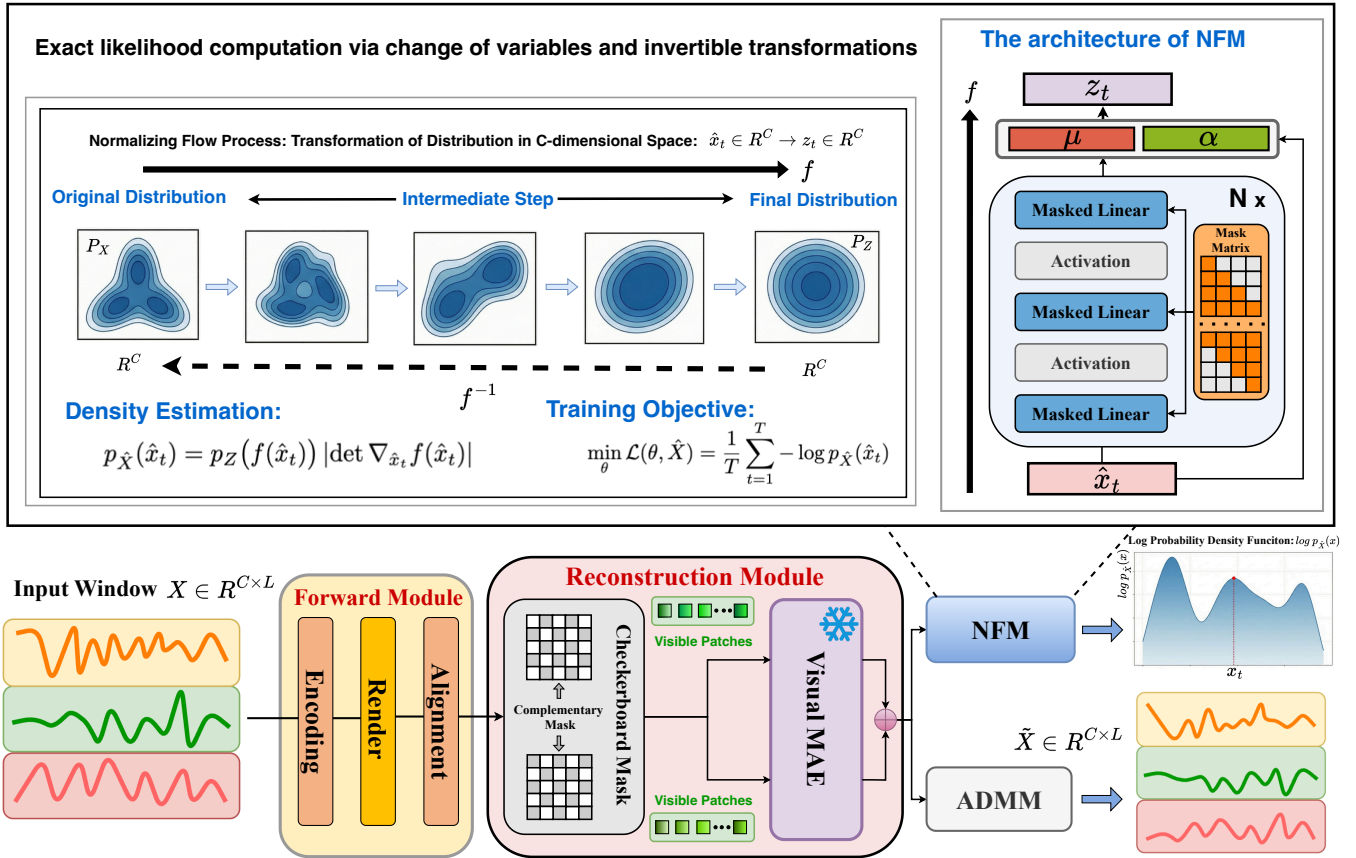


Fig. 2: The overall architecture of VAN-AD. (1) Forward Module: transforms the input time series into a format compatible with MAE. (2) Reconstruction Module: generates a pair of complementary masked images using the Checkerboard Mask strategy, and reconstructs the masked regions through MAE to obtain the reconstructed time series. (3) ADMM: maps the reconstructed sequence into the statistical space of the original sequence to amplify reconstruction discrepancies. (4) NFM: applies normalizing flow to the reconstructed sequence to model the probability density of the current window.

A. Time Series Anomaly Detection

Given a multivariate time series $X = (x_1, x_2, \dots, x_T) \in \mathbb{R}^{T \times C}$, where T is the sequence length and C is the number of variables, time series anomaly detection aims to predict an anomaly label sequence $Y = (y_1, y_2, \dots, y_T) \in \{0, 1\}^T$, where y_t indicates whether the observation x_t at time step t is anomalous.

B. Visual Masked Autoencoders

MAE [13] is a computer vision foundation model pretrained on ImageNet [34] in a self-supervised manner. Its core idea is to learn image representations through a mask and reconstruct pretext task. Specifically, the input image I is first divided into a sequence of non-overlapping patches, after which a very high masking ratio (typically up to 75%) is applied so that only a small subset of visible patches is retained as input to the encoder. This asymmetric design is central to MAE: the encoder processes only the visible patch sequence and maps it into a latent feature space, while the decoder takes the encoded latent representations together with mask tokens indicating the missing positions and attempts to reconstruct the

pixel values of the original image. By minimizing the mean squared error (MSE) between the reconstructed output and the original image over the masked regions during training, MAE is encouraged not only to capture local details but also to infer missing information from the global contextual structure.

As an image reconstruction and completion model, MAE can be naturally adapted as a numerical sequence reconstructor. This characteristic is closely aligned with the intuition behind reconstruction-based anomaly detection methods. Therefore, in this work, we investigate the potential of MAE for TSAD.

C. Normalizing Flow

Normalizing Flow is an unsupervised density estimation technique that transforms a complex data distribution into a simple latent distribution through a sequence of invertible transformations [35], [36]. Its core idea is to achieve exact likelihood modeling of the target data based on the change of variables theorem.

Let the observed variable $x \in \mathbb{R}^d$ follow an unknown distribution $p_X(x)$. Normalizing Flow defines a bijective function

$f : \mathcal{X} \rightarrow \mathcal{Z}$, which maps x to a latent variable $z \in \mathbb{R}^d$ following a known simple distribution, such as a standard Gaussian distribution $p_Z(z) = \mathcal{N}(0, I)$, i.e., $z = f(x)$.

According to the change of variables theorem, the probability density of the observed data x can be written as

$$p_X(x) = p_Z(f(x)) |\det \nabla_x f(x)|, \quad (1)$$

where $\nabla_x f(x)$ denotes the Jacobian matrix of the transformation f at x .

To enhance the representational capacity of the model, the transformation f is usually composed of K simple invertible layers, i.e.,

$$f = f_K \circ f_{K-1} \circ \dots \circ f_1.$$

Let $z_0 = x$ and $z_K = z$. Then, the log-likelihood of the overall transformation can be expressed as

$$\log p_X(x) = \log p_Z(z_K) + \sum_{k=1}^K \log |\det \nabla_{z_{k-1}} f_k(z_{k-1})|. \quad (2)$$

This mechanism enables the model to capture the distributional characteristics of normal observations by directly maximizing their log-likelihood.

IV. METHODOLOGY

This section overviews the architecture of VAN-AD and then details each modules in the model.

A. Overview

Fig. 2 illustrates the overall architecture of VAN-AD. Given a multivariate time series $X \in \mathbb{R}^{C \times L}$, we first transform it into a two dimensional image through the Forward Module and construct a pair of complementary masked images using Checkerboard Masking. A pretrained visual MAE is then applied to recover the masked regions, and the reconstructed image is subsequently converted back into a multivariate time series. To enlarge the discrepancy between the original and reconstructed sequences, we further introduce ADMM, which maps the reconstructed sequence into the statistical space of the original sequence. Meanwhile, NFM is designed to model the probability density of normal patterns, allowing the model to incorporate the density of the current window under the global distribution into anomaly detection.

B. The Forward Module

To preserve variable information in multivariate time series, we adopt a heatmap encoding strategy. Specifically, the input time series X is first represented as $I_{\text{raw}} \in \mathbb{R}^{C \times L}$. To make it compatible with the pretrained MAE, we then render I_{raw} as a grayscale image $I_{\text{gray}} \in \mathbb{R}^{C \times L \times 3}$ by replicating I_{raw} across all three channels. Since the pretrained MAE uses a fixed input resolution of 224×224 , I_{gray} is further resized to this resolution through bilinear interpolation, yielding the final input image $I \in \mathbb{R}^{224 \times 224 \times 3}$.

C. The Reconstruction Module

In this paper, we adopt a checkerboard masking strategy to construct a pair of complementary masked images. Each image is reconstructed from its visible regions, allowing the model to more fully capture both temporal dependencies and inter-variable correlations.

Specifically, the input image I is first divided into a set of non-overlapping patches. Let the patch size be $P \times P$. The image is then partitioned into an $N \times N$ grid, where $N = 224/P$. Each patch is indexed by coordinates (i, j) , where $i, j \in \{0, 1, \dots, N-1\}$. Based on this patch grid, we define a checkerboard mask as

$$M(i, j) = \begin{cases} 1, & \text{if } (i+j) \text{ is even,} \\ 0, & \text{if } (i+j) \text{ is odd,} \end{cases} \quad \bar{M}(i, j) = 1 - M(i, j), \quad (3)$$

where M and \bar{M} form a pair of complementary masks.

Using these two masks, we construct a pair of complementary masked images, denoted by $I^{(1)}$ and $I^{(2)}$:

$$I^{(1)} = I \odot M, \quad I^{(2)} = I \odot \bar{M}, \quad (4)$$

where \odot denotes the patch-wise masking operation. In other words, $I^{(1)}$ preserves the patches whose indices satisfy that $(i+j)$ is even, while $I^{(2)}$ preserves the complementary set of patches.

The two masked images are then separately fed into the pretrained MAE to reconstruct the missing regions:

$$R^{(1)} = \text{MAE}(I^{(1)}), \quad R^{(2)} = \text{MAE}(I^{(2)}), \quad (5)$$

where $R^{(1)}$ and $R^{(2)}$ denote the reconstructed full images. Since the two masked images retain complementary visible regions, their reconstructed outputs are fused to obtain the final reconstructed image R .

Finally, the reconstructed image R is resized back to the original multivariate time series resolution through bilinear interpolation, yielding the reconstructed sequence $\hat{X} \in \mathbb{R}^{C \times L}$.

D. The Adaptive Distribution Mapping Module

Directly applying MAE for reconstruction suffers from an over-generalization issue. Although X and \hat{X} may be close in numerical values, they often differ in their statistical characteristics. In particular, the MAE output is usually smoother and exhibits weaker local variability than the original sequence.

To better expose the discrepancy before and after reconstruction, we design an Adaptive Distribution Mapping Module (ADMM). Specifically, given the original sequence $X \in \mathbb{R}^{C \times L}$ and the reconstructed sequence $\hat{X} \in \mathbb{R}^{C \times L}$, we first compute the variable-wise mean and standard deviation of X as

$$\mu_c = \frac{1}{L} \sum_{t=1}^L X_{c,t}, \quad \sigma_c = \sqrt{\frac{1}{L} \sum_{t=1}^L (X_{c,t} - \mu_c)^2 + \epsilon}, \quad (6)$$

where ϵ is a small constant for numerical stability.

We then map the reconstructed sequence \hat{X} into the statistical space of the original sequence, yielding the adjusted

reconstruction \tilde{X} :

$$\tilde{X}_{c,t} = \hat{X}_{c,t} \cdot \sigma_c + \mu_c. \quad (7)$$

In this way, ADMM aligns the reconstructed sequence with the statistical characteristics of the original input, providing a more reliable basis for discrepancy estimation. As a result, deviations caused by abnormal patterns become more distinguishable.

E. The Normalizing Flow Module

While ADMM is introduced to amplify the discrepancy between the original and reconstructed sequences, we further observe that the reconstructed sequence is typically smoother and less noisy than the original input. This property makes it a more suitable basis for modeling the distribution of normal patterns. Based on this observation, we employ a normalizing flow on top of the reconstructed sequence to estimate the global probability density of the current window.

For each reconstructed observation $\hat{x}_t \in \mathbb{R}^C$, a normalizing flow $f : \mathbb{R}^C \rightarrow \mathbb{R}^C$ is used to model the corresponding density $p_{\hat{X}}(\hat{x}_t)$. Specifically, \hat{x}_t is mapped to a latent variable $z_t = f(\hat{x}_t)$. The base density is defined as a Gaussian distribution with mean vector $u \in \mathbb{R}^C$ and identity covariance, i.e., $p_Z(z_t) = \mathcal{N}(z_t | u, I)$, where u is randomly initialized once at model initialization and then kept fixed.

Inspired by MAF [37], we adopt Masked Autoregressive Flow as the normalizing flow architecture. As illustrated in Fig. 2, the flow f consists of N stacked layers, each composed of a Masked Linear transformation followed by an activation function. To capture dependencies among variables more effectively, the causal dependency matrix is reversed at each layer, so that every variable can progressively interact with all other variables throughout the flow.

Consider an autoregressive model whose conditional distributions are parameterized as univariate Gaussians. The i th conditional distribution is defined as

$$p(\hat{x}_{t,i} | \hat{x}_{t,1:i-1}) = \mathcal{N}(\hat{x}_{t,i} | \mu_i, (\exp \alpha_i)^2), \quad (8)$$

where $\mu_i = f_{\mu_i}(\hat{x}_{t,1:i-1})$ and $\alpha_i = f_{\alpha_i}(\hat{x}_{t,1:i-1})$.

After estimating μ_i and α_i , the transformation from \hat{x}_t to z_t is given by

$$z_{t,i} = [f(\hat{x}_t)]_i = (\hat{x}_{t,i} - \mu_i) \exp(-\alpha_i). \quad (9)$$

Due to the autoregressive structure, the Jacobian matrix of f is triangular. Therefore, its absolute determinant can be efficiently computed as

$$|\det \nabla_{\hat{x}_t} f(\hat{x}_t)| = \exp\left(-\sum_{i=1}^C \alpha_i\right). \quad (10)$$

Accordingly, the log density of \hat{x}_t can be written as

$$\begin{aligned} \log p_{\hat{X}}(\hat{x}_t) &= \log p_Z(f(\hat{x}_t)) + \log |\det \nabla_{\hat{x}_t} f(\hat{x}_t)| \\ &= -\frac{1}{2} \sum_{i=1}^C \left[(z_{t,i} - u_i)^2 + \log 2\pi \right] - \sum_{i=1}^C \alpha_i. \end{aligned} \quad (11)$$

Algorithm 1 Inference procedure of VAN-AD

Input: Multivariate time series window $X \in \mathbb{R}^{C \times L}$, pre-trained MAE, Normalizing Flow model f , trade-off parameter λ

Output: Anomaly scores $\{S_t\}_{t=1}^L$

- 1: Convert X into a 2D image I
 - 2: Generate complementary masked images $I^{(1)}$ and $I^{(2)}$ via Checkerboard Masking
 - 3: **for** $k = 1$ to 2 **do**
 - 4: Reconstruct $I^{(k)}$ with MAE to obtain the reconstructed image $R^{(k)}$
 - 5: **end for**
 - 6: Fuse $R^{(1)}$ and $R^{(2)}$ to obtain the complete reconstructed image R
 - 7: Resize R back to the original time-series resolution to obtain $\hat{X} \in \mathbb{R}^{C \times L}$
 - 8: Compute μ_c and σ_c for each variable c of the original sequence
 - 9: Apply ADMM to obtain \tilde{X} , where $\tilde{X}_{c,t} = \hat{X}_{c,t} \cdot \sigma_c + \mu_c$
 - 10: **for** $t = 1$ to L **do**
 - 11: $S_{\text{MAE}}^{(t)} = \|\tilde{x}_t - x_t\|_2^2$
 - 12: $S_{\text{NF}}^{(t)} = -\log p_{\hat{X}}(x_t)$
 - 13: $S_t = S_{\text{MAE}}^{(t)} + \lambda S_{\text{NF}}^{(t)}$
 - 14: **end for**
 - 15: **return** $\{S_t\}_{t=1}^L$
-

F. Training Objective

Since the pretrained MAE is used only during inference for TSAD, it remains frozen throughout training, and only the normalizing flow is optimized. In standard normalizing flow training, the objective is to maximize the likelihood of the observed data, which is equivalent to minimizing the Kullback–Leibler divergence between the true data distribution and the distribution induced by the flow. Accordingly, the training objective is defined as

$$\min_{\theta} \mathcal{L}(\theta, \hat{X}) = \frac{1}{T} \sum_{t=1}^T -\log p_{\hat{X}}(\hat{x}_t), \quad (12)$$

where θ denotes the parameters of the normalizing flow.

G. Anomaly Detection

Based on the assumption that anomalous data are difficult to reconstruct, we use the reconstruction discrepancy before and after MAE to quantify the anomaly score at each time step. In addition, since anomalies usually deviate from the majority of data instances, they are also expected to have lower probability density under the learned normal pattern distribution. Therefore, we further incorporate the density estimated by the normalizing flow as an additional anomaly indicator, where lower density implies a higher likelihood of anomaly.

Specifically, the original observation x_t is evaluated under the flow based distribution learned from the reconstructed

TABLE I: Statistics of the datasets.

Dataset	Domain	Variable	Train Length	Test Length	Description
Callt2	Visitors Flowrate	2	2,520	2,520	Building entry/exit count time series (15 days)
CICIDS	Web Traffic	72	85,115	82,116	Network traffic data with 80+ features and attack lab
DLR	Health	19	11,565	11,565	Physiological time series with anomalies from monitoring systems
GECCO	Water Treatment	9	69,260	69,261	Water treatment data from the GECCO Challenge
MSL	Spacecraft	1	58,317	73,729	Spacecraft telemetry and anomaly data from the MSL rover
NYC	Transport	3	13,104	4,416	Information on taxi and ride-hailing trips in New York
PUMP	Water Treatment	44	76,901	14,3401	Sensor data from pump systems in water treatment processes
PSM	Server Machine	25	13,2481	87,841	Application server telemetry data with labeled anomalies
SWAN	Space Weather	38	60,000	60,000	Space weather data (satellite and geomagnetic measurements)

sequence. The anomaly score at time step t is defined as

$$S_t = S_{MAE}^{(t)} + \lambda S_{NF}^{(t)}, \quad (13)$$

where

$$S_{MAE}^{(t)} = \|\tilde{x}_t - x_t\|_2^2, \quad (14)$$

$$S_{NF}^{(t)} = -\log p_{\hat{X}}(x_t), \quad (15)$$

and λ controls the contribution of the density based anomaly score estimated by the normalizing flow. The detailed inference procedure is presented in Algorithm 1.

V. EXPERIMENTS

A. Datasets

We evaluate VAN-AD on nine real-world datasets: Callt2, CICIDS, DLR, GECCO, MSL, NYC, PUMP, PSM, and SWAN. These datasets are widely used in TSAD and cover a diverse range of application domains. Detailed dataset statistics are reported in Table I.

B. Baselines

We compare VAN-AD with 15 baseline methods, including TS-based methods, Text-based methods, recent deep learning baselines, and classical anomaly detection methods. Specifically, the TS-based methods include DADA [7] and Timer [26], while the Text-based methods include CALF [38] and GPT4TS [27]. We also include several recent deep learning baselines, including CATCH [4], MtsCID [21], CAROTS [23], iTransformer (iTrans) [39], ModernTCN (Modern) [40], DualTF [41], and ContraAD [42]. In addition, several classical anomaly detection methods are considered, including Local Outlier Factor (LOF) [16], Cluster-based Local Outlier Factor (CBLOF) [17], K-th Nearest Neighbor (KNN) [19] and Principal Component Analysis (PCA) [18].

C. Setup

1) *Metrics*: Recent studies have shown that the point adjustment strategy widely used in time series anomaly detection may produce overly optimistic results, and can even yield state-of-the-art performance when applied to random methods [43]. To address this issue, some studies have adopted Affiliation-F1 [44], which measures recall by considering the average directional distance between predicted events and ground-truth events. However, TSB-AD [45] points out that

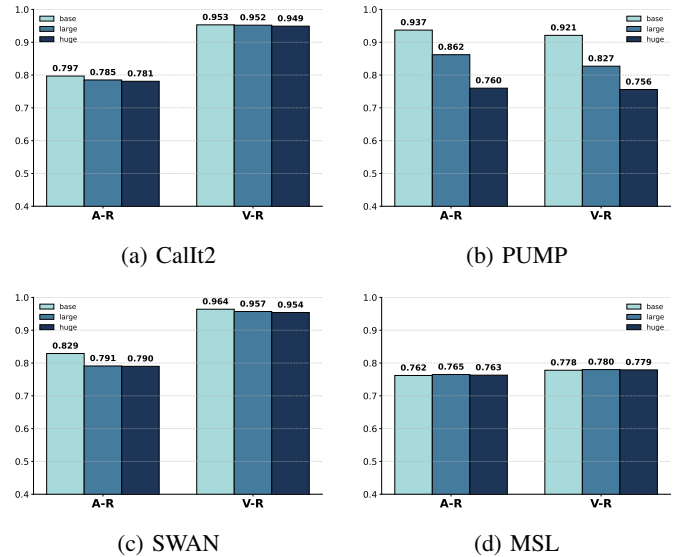


Fig. 3: Backbone analysis of MAE variants with different model sizes (base, large, and huge), evaluated by A-R and V-R.

Affiliation-F1 has limited discriminative ability and cannot effectively reflect differences in prediction quality. Therefore, we adopt threshold-independent evaluation metrics, including the Area Under the Receiver Operating Characteristic Curve (AUC-ROC), Area Under the Precision-Recall Curve (AUC-PR), Volume Under the Surface-Receiver Operating Characteristic (VUS-ROC), and Volume Under the Surface-Precision-Recall (VUS-PR).

2) *Implementation Details*: In our experiments, we use the MAE-base model (112M) as the visual backbone. For the normalizing flow, the default batch size is set to 128 and is reduced by half when out-of-memory (OOM) errors occur. We use tanh as the activation function because its smooth and bounded nature helps maintain numerical stability, and set the number of flow layers N to 3 by default. Unless otherwise specified, all datasets are trained for 5 epochs with a learning rate of 0.005.

We reimplement and run DADA, Timer, CALF, GPT4TS, MtsCID, and CAROTS using their publicly available optimal parameter settings to ensure a fair comparison. For the remaining baseline models, we report the results from TAB [46].

All experiments are conducted on a single NVIDIA A800

TABLE II: A-R (AUC-ROC), A-P (AUC-PR), V-R (VUS-ROC), and V-P (VUS-PR) results on nine real-world datasets, where higher values indicate better performance. The best results are highlighted in bold, and the second-best results are underlined.

Dataset	Metric	VAN-AD	DADA	Timer	CALF	GPT4TS	CATCH	MtsCID	CAROTS	iTrans	Modern	DualTF	ContraAD	LOF	CBLOF	KNN	PCA
Call2	A-R	0.797	0.759	0.739	0.614	0.731	0.772	0.610	0.767	<u>0.791</u>	0.691	0.421	0.472	0.509	0.772	0.539	0.790
	A-P	<u>0.108</u>	0.090	0.079	0.052	0.082	0.089	0.048	0.188	0.106	0.063	0.029	0.026	0.035	0.093	0.037	0.073
	V-R	0.953	0.796	0.785	0.668	0.766	0.796	0.643	<u>0.903</u>	0.809	0.740	0.431	0.425	0.532	0.808	0.514	0.786
	V-P	0.414	0.096	0.096	0.060	0.087	0.101	0.326	<u>0.375</u>	0.110	0.079	0.041	0.040	0.061	0.111	0.101	0.103
CICIDS	A-R	0.700	0.682	0.679	0.617	<u>0.712</u>	0.669	0.500	0.580	0.668	0.670	0.543	0.453	0.458	0.804	0.564	0.601
	A-P	0.007	0.001	0.001	0.001	0.002	0.001	0.001	0.007	0.001	0.001	0.002	0.001	0.001	0.002	0.001	0.001
	V-R	0.926	0.641	0.647	0.518	0.660	0.598	0.507	0.722	0.578	0.622	0.416	0.327	0.332	<u>0.773</u>	0.465	0.496
	V-P	0.020	0.002	0.002	0.001	0.002	0.002	0.020	0.015	0.002	0.002	0.001	0.001	0.001	0.003	0.001	0.001
DLR	A-R	0.990	0.948	0.907	0.900	0.902	0.922	0.497	0.744	0.951	<u>0.961</u>	0.902	0.108	0.396	0.880	0.889	0.911
	A-P	0.704	0.170	0.238	0.193	0.108	0.171	0.015	0.035	0.194	0.289	0.072	0.008	0.007	0.075	0.070	<u>0.295</u>
	V-R	0.994	0.940	0.939	0.930	0.899	0.921	0.496	0.785	0.933	0.957	0.939	0.248	0.473	0.874	0.885	<u>0.960</u>
	V-P	0.693	0.190	<u>0.357</u>	0.175	0.091	0.161	0.013	0.041	0.169	0.206	0.198	0.010	0.060	0.071	0.072	0.329
GECCO	A-R	0.978	0.772	<u>0.955</u>	0.866	0.836	0.912	0.535	0.507	0.780	0.954	0.613	0.537	0.796	0.684	0.811	0.711
	A-P	0.619	0.264	<u>0.482</u>	0.189	0.162	0.198	0.019	0.147	0.081	0.437	0.062	0.014	0.086	0.072	0.170	0.234
	V-R	0.996	0.706	0.935	0.930	0.908	0.953	0.514	0.477	0.852	<u>0.971</u>	0.649	0.558	0.767	0.678	0.756	0.595
	V-P	0.722	0.046	0.305	0.235	0.256	0.260	0.038	0.038	0.107	<u>0.431</u>	0.045	0.020	0.058	0.038	0.068	0.046
MSL	A-R	0.762	0.547	<u>0.637</u>	0.592	0.594	0.627	0.500	0.557	0.589	0.621	0.499	0.548	0.557	0.622	0.623	0.552
	A-P	0.293	0.138	0.155	0.143	0.137	0.154	0.106	0.154	0.141	0.145	0.114	0.111	0.120	0.181	<u>0.200</u>	0.157
	V-R	0.778	0.630	<u>0.700</u>	0.669	0.665	0.699	0.511	0.612	0.668	0.693	0.593	0.636	0.617	0.684	0.642	0.622
	V-P	0.297	0.200	0.229	0.215	0.199	0.229	0.150	0.167	0.217	0.221	0.173	0.167	0.181	0.224	<u>0.242</u>	0.200
NYC	A-R	0.857	0.659	0.661	0.457	0.495	0.469	0.515	0.519	0.594	0.696	<u>0.723</u>	0.443	0.464	0.528	0.466	0.666
	A-P	0.092	0.035	0.034	0.020	0.027	0.021	0.023	0.026	0.030	<u>0.046</u>	0.045	0.020	0.020	0.024	0.020	0.042
	V-R	0.873	0.689	0.704	0.573	0.628	0.593	0.530	0.622	0.663	0.716	<u>0.739</u>	0.580	0.581	0.641	0.608	0.730
	V-P	0.318	0.051	0.054	0.042	0.052	0.040	0.043	0.039	0.048	0.060	0.059	0.038	0.049	0.052	0.051	<u>0.072</u>
PUMP	A-R	0.937	0.788	0.529	0.523	0.414	0.466	0.500	0.785	0.577	0.420	0.605	0.656	0.479	0.621	0.524	<u>0.802</u>
	A-P	0.559	0.199	0.139	0.126	0.101	0.104	0.102	<u>0.210</u>	0.123	0.111	0.115	0.147	0.089	0.118	0.104	0.209
	V-R	0.921	0.789	0.712	0.644	0.551	0.583	0.500	0.779	0.668	0.642	0.684	0.537	0.605	0.605	0.536	<u>0.793</u>
	V-P	0.571	0.228	<u>0.260</u>	0.210	0.177	0.168	0.107	0.208	0.190	0.205	0.152	0.180	0.127	0.155	0.138	0.248
PSM	A-R	0.815	0.621	0.556	0.583	0.584	0.600	0.500	<u>0.767</u>	0.583	0.587	0.544	0.533	0.730	0.717	0.744	0.667
	A-P	0.622	0.448	0.359	0.369	0.380	0.385	0.280	0.537	0.372	0.388	0.311	0.298	0.462	0.529	<u>0.553</u>	0.477
	V-R	0.817	0.599	0.541	0.579	0.579	0.600	0.515	<u>0.750</u>	0.582	0.584	0.496	0.438	0.641	0.636	0.667	0.576
	V-P	0.661	0.423	0.350	0.370	0.379	0.389	0.320	<u>0.529</u>	0.376	0.387	0.308	0.297	0.423	0.442	0.456	0.413
SWAN	A-R	0.829	0.645	0.624	0.515	0.503	0.485	0.500	0.613	0.512	0.519	0.608	0.561	0.740	0.889	<u>0.878</u>	0.666
	A-P	0.687	0.550	0.511	0.411	0.454	0.425	0.329	0.846	0.419	0.454	0.446	0.502	0.598	<u>0.770</u>	0.764	0.544
	V-R	0.964	0.561	0.547	0.425	0.447	0.415	0.803	<u>0.807</u>	0.435	0.456	0.430	0.418	0.601	0.744	0.798	0.483
	V-P	0.924	0.487	0.461	0.376	0.407	0.376	0.838	<u>0.904</u>	0.382	0.406	0.405	0.418	0.517	0.711	0.696	0.448
Average	A-R	0.852	0.713	0.698	0.630	0.641	0.658	0.517	0.649	0.672	0.680	0.606	0.479	0.570	<u>0.724</u>	0.671	0.707
	A-P	0.409	0.255	0.228	0.178	0.183	0.192	0.123	<u>0.329</u>	0.170	0.215	0.133	0.125	0.159	0.239	0.213	0.227
	V-R	0.913	0.705	0.699	0.659	0.678	0.684	0.554	0.736	0.659	0.702	0.622	0.459	0.612	<u>0.742</u>	0.652	0.669
	V-P	0.595	0.253	0.260	0.209	0.227	0.231	0.327	<u>0.405</u>	0.222	0.244	0.192	0.176	0.205	0.248	0.203	0.206

GPU with 40 GB of memory to minimize the influence of platform-related factors.

D. Main Results

We conduct extensive evaluations on nine real-world datasets against 15 competitive baselines, as reported in Table II. The results show that VAN-AD achieves the best overall performance across the evaluated datasets. This suggests that VAN-AD can effectively distinguish normal samples from anomalous ones and maintain strong detection capability under threshold-independent evaluation metrics, which is particularly important in practical applications. Compared with 2025 SOAT CATCH [4], VAN-AD improves the average A-R, A-P, V-R, and V-P scores by 19.4%, 21.7%, 22.9%, and 36.4%, respectively. Moreover, compared with TS-based and Text-based methods, VAN-AD achieves clear advantages on most datasets, which supports the effectiveness of transferring large vision models to time series anomaly detection.

We also observe that on some datasets, such as CICIDS and SWAN, classical methods outperform deep learning based

methods. This observation is consistent with the conclusion of TSB-AD [45], which suggests that classical time series anomaly detection methods remain competitive and that simpler statistical methods can sometimes yield better performance. This finding also provides useful insights for future research.

E. Ablation Study

As shown in Table III, we further evaluate the contribution of each component in VAN-AD. Removing ADMM consistently degrades performance, indicating that directly using a pretrained MAE for anomaly detection is prone to the over-generalization issue. Since MAE is pretrained on large-scale image data, it may reconstruct relatively simple time series patterns excessively well, thereby reducing the discrepancy between normal and anomalous points. ADMM alleviates this issue by amplifying the discrepancy before and after reconstruction.

Similarly, removing NFM also leads to performance drops across datasets. This suggests that reconstruction based only

TABLE III: Ablation studies for VAN-AD. The A-R, A-P, V-R, and V-P denote AUC-ROC, AUC-PR, VUS-ROC, and VUS-PR, respectively, where higher values indicate better performance. The best ones are highlighted in bold. Specifically, the zero-shot setting is equivalent to removing both ADMM and NFM simultaneously, that is, directly applying MAE for inference.

Dataset	Callt2				MSL				PSM				SWAN				PUMP			
	A-R	A-P	V-R	V-P	A-R	A-P	V-R	V-P	A-R	A-P	V-R	V-P	A-R	A-P	V-R	V-P	A-R	A-P	V-R	V-P
zero-shot	0.759	0.068	0.933	0.290	0.610	0.206	0.672	0.223	0.635	0.494	0.655	0.480	0.524	0.483	0.939	0.896	0.809	0.216	0.806	0.231
w/o ADMM	0.794	0.089	0.945	0.326	0.588	0.203	0.645	0.217	0.766	0.581	0.763	0.562	0.827	0.684	0.963	0.920	0.935	0.557	0.917	0.533
w/o NF	0.788	0.108	0.947	0.412	0.755	0.277	0.773	0.288	0.717	0.527	0.745	0.585	0.701	0.597	0.949	0.918	0.466	0.134	0.479	0.142
VAN-AD	0.797	0.108	0.953	0.414	0.762	0.293	0.778	0.297	0.815	0.622	0.817	0.661	0.829	0.687	0.964	0.924	0.937	0.559	0.921	0.538

TABLE IV: Comparison of time series encoding methods.

Method	TS-Type	Description	Advantages and limitations
Seg	UTS	Rearranges time series segments into a two-dimensional layout	Preserves local temporal order with simple construction, but is weak in modeling global structure
GAF	UTS	Encodes pairwise temporal correlations into a two dimensional matrix	Captures pairwise temporal correlations in a visually structured form, but is costly for multivariate data
STFT	UTS	Produces a two dimensional time-frequency representation through the short time Fourier transform	Captures frequency patterns and local spectral changes, but has limited time-frequency resolution
Wavelet	UTS	Generates a two dimensional time-frequency representation via wavelet decomposition	Captures local details and multi-scale patterns, but is sensitive to wavelet choice
RP	UTS	Visualizes recurrence relationships in reconstructed phase space as a two dimensional matrix	Reveals recurrent structures and nonlinear dynamics, but is computationally expensive for long sequences
Heatmap	UTS, MTS	Represents a multivariate time series as a variable-time matrix	Enables efficient inference, but provides limited explicit modeling of frequency information

on MAE is insufficient when anomalies span a long duration and cannot be fully characterized within the current window. In such cases, the model may treat the local variation within the window as normal due to the lack of global context. By contrast, NFM captures the probability density of the current window under the global distribution and combines this information with the MAE reconstruction result to improve anomaly detection.

When both ADMM and NFM are removed, the resulting variant degenerates into directly applying MAE in a zero-shot manner. Combined with the results in Table II, this variant performs worse than the other baselines. This indicates that, although image data and time series data share certain structural similarities, a model pretrained on image data cannot be directly transferred to TSAD without a clear performance gap. These results further demonstrate the effectiveness of the proposed modules in adapting MAE to TSAD.

F. Further Analysis of MAE for TSAD

1) *Backbone Analysis*: Fig. 3 compares the anomaly detection performance of three MAE variants with different parameter scales (112M, 330M, and 657M). It can be observed that increasing the model size does not lead to better TSAD performance, and even results in a slight decline. A possible reason is that larger vision models tend to overfit image-specific features, thereby reducing their transferability, which is consistent with the findings reported in VisionTS [10].

2) *Imaging Analysis*: Existing studies summarize six mainstream encoding strategies for time series representation [32], namely Segment (Seg), Gramian Angular Field (GAF), STFT,

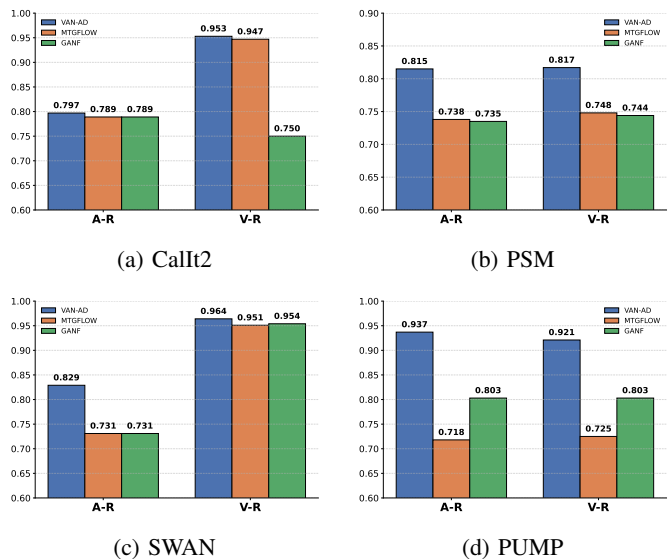


Fig. 4: Density modeling analysis evaluated by A-R and V-R. The compared methods include VAN-AD, MTGFLOW, and GANF.

Wavelet, Recurrence Plot (RP), and Heatmap. These methods differ in whether they emphasize temporal layout, temporal correlations, time-frequency characteristics, dynamical structure, or direct variable-time representation. Detailed descriptions of the six encoding strategies are provided in Table IV.

The experimental results for different encoding strategies are shown in Table V. We observe that different encoding methods have limited impact on the V-R and V-P metrics,

TABLE V: Imaging experiments for VAN-AD, evaluated by V-R and V-P. And time indicates the duration required to process the entire test dataset. The best ones are in bold.

Dataset	PSM			PUMP			SWAN		
	V-R	V-P	Time(s)	V-R	V-P	Time(s)	V-R	V-P	Time(s)
Seg	0.801	0.651	37.51	0.802	0.224	210.29	0.961	0.918	38.97
GAF	0.804	0.648	37.42	0.956	0.535	209.67	0.958	0.926	38.99
STFT	0.621	0.384	37.30	0.807	0.222	209.55	0.943	0.891	39.01
Wavelet	0.528	0.322	37.58	0.768	0.189	210.75	0.965	0.920	39.51
RP	0.561	0.332	37.30	0.520	0.098	209.61	0.951	0.923	38.99
Heatmap	0.817	0.661	2.49	0.921	0.538	5.07	0.964	0.924	1.17

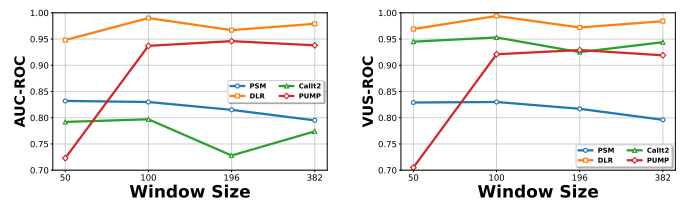
TABLE VI: Comparison of different flow architectures. Linear denotes that the linear layer is implemented as a fully connected layer, whereas Masked Linear denotes the architecture adopted in our method.

Dataset	Callt2		PSM		PUMP		SWAN	
	V-R	V-P	V-R	V-P	V-R	V-P	V-R	V-P
Linear	0.953	0.412	0.742	0.516	0.781	0.208	0.950	0.890
Masked Linear	0.953	0.414	0.817	0.661	0.921	0.538	0.964	0.924

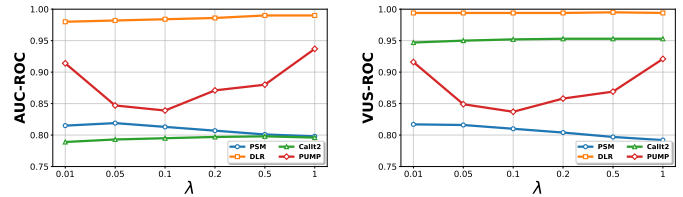
but result in substantial differences in inference time. This is because, except for Heatmap, the other methods are primarily designed for univariate time series and therefore require channel-independent inference. As a result, the computational cost increases significantly when the number of variables is large, as in datasets such as PSM, PUMP, and SWAN. Considering the importance of inference efficiency in real-world applications, we adopt Heatmap because it is naturally suited to multivariate time series encoding and achieves a better trade-off between detection performance and computational cost.

3) *Fine-tuning Analysis*: We further evaluate the effect of jointly fine-tuning MAE during training, whereas in the previous setting the MAE remains frozen. Five fine-tuning strategies are considered: (1) *ln*, which fine-tunes the layer normalization layers; (2) *bias*, which updates only the bias terms; (3) *attn*, which fine-tunes only the self-attention related parameters; (4) *mlp*, which fine-tunes only the feed-forward network components in the Transformer blocks; and (5) *full*, which fine-tunes all MAE parameters. The learning rate for MAE fine-tuning is set to 0.005 by default, and each dataset is fine-tuned for 5 epochs. The results are reported in Table VII.

We observe that fine-tuning has limited effect on datasets with relatively few variables, such as Callt2 and MSL. In contrast, on high dimensional datasets, fine-tuning consistently degrades performance. One possible explanation is that datasets with more variables exhibit more complex inter-variable dependencies, which makes MAE more likely to overfit dataset patterns during fine-tuning. As a result, the transferable visual priors learned during pretraining are weakened, and the separability between normal and anomalous patterns is reduced.



(a) Window Size



(b) Lambda

Fig. 5: Parameter sensitivity studies of main hyper-parameters in VAN-AD.

G. Further Analysis of Normalizing Flow

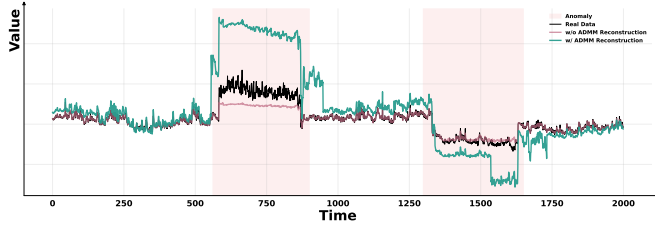
1) *Density Modeling Analysis*: We further evaluate the effectiveness of NFM by replacing it with the flow designs adopted in GANF and MTGFLOW. Unlike our method, which jointly models each $\hat{x}_t \in \mathbb{R}^C$ using $f : \mathbb{R}^C \rightarrow \mathbb{R}^C$, both GANF and MTGFLOW perform variable-independent density estimation with $f : \mathbb{R} \rightarrow \mathbb{R}$. As shown in Fig. 4, both replacements result in inferior performance. This suggests that joint density modeling over all variables is more suitable for TSAD, since it captures inter-variable dependencies that are important for detecting anomalies caused by abnormal variable interactions.

2) *Base Density Analysis*: In this paper, we define the base density as a Gaussian distribution with mean vector $u \in \mathbb{R}^C$ and identity covariance, i.e., $p_Z(z_t) = \mathcal{N}(z_t | u, I)$, where u is randomly initialized once at model initialization and then kept fixed. To examine the effect of this design, we replace the randomly initialized Gaussian prior with a fixed standard Gaussian prior, i.e., $p_Z(z_t) = \mathcal{N}(z_t | 0, I)$. As shown in Table VIII, the two settings perform similarly on datasets with relatively few variables, such as Callt2, whereas random initialization consistently performs better on high dimensional datasets, with particularly notable gains on PSM and PUMP. One possible explanation is that, when the number of variables is small, the joint distribution is relatively simple, so both priors provide comparable alignment targets for the flow. By contrast, for high dimensional multivariate data, a fixed zero-centered prior imposes a stronger constraint on latent alignment, while random initialization offers a more flexible anchor for the reversible mapping, thereby facilitating optimization and better preserving inter-variable structure.

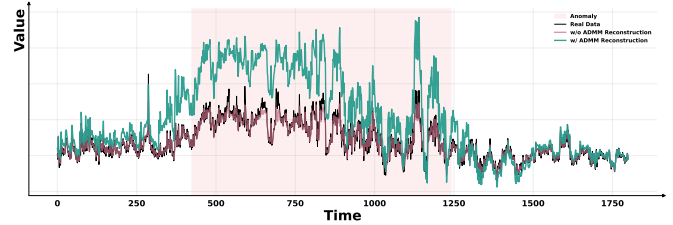
3) *The Flow f Analysis*: We also evaluate the effect of the flow architecture by replacing the Masked Linear layers with fully connected linear layers. As shown in Table VI, this replacement has little effect on datasets with relatively few variables, such as Callt2, but leads to more obvious performance degradation on datasets with many variables. This

TABLE VII: Finetune experiments for VAN-AD. The best ones are in bold.

Dataset	Callt2				MSL				PSM				PUMP				SWAN			
	A-R	A-P	V-R	V-P	A-R	A-P	V-R	V-P	A-R	A-P	V-R	V-P	A-R	A-P	V-R	V-P	A-R	A-P	V-R	V-P
In	0.779	0.097	0.952	0.417	0.767	0.262	0.811	0.294	0.655	0.378	0.650	0.396	0.596	0.110	0.596	0.113	0.626	0.480	0.931	0.868
bias	0.763	0.096	0.952	0.417	0.679	0.225	0.736	0.252	0.626	0.347	0.629	0.370	0.782	0.185	0.779	0.200	0.450	0.333	0.900	0.823
attn	0.760	0.094	0.946	0.345	0.685	0.225	0.729	0.258	0.664	0.382	0.637	0.401	0.485	0.092	0.491	0.092	0.566	0.440	0.925	0.852
mlp	0.802	0.092	0.938	0.269	0.749	0.253	0.788	0.283	0.633	0.335	0.596	0.369	0.459	0.084	0.460	0.086	0.635	0.508	0.936	0.874
full	0.772	0.094	0.939	0.280	0.674	0.237	0.720	0.266	0.652	0.356	0.626	0.387	0.803	0.205	0.804	0.205	0.744	0.656	0.955	0.910
VAN-AD	0.797	0.108	0.953	0.414	0.762	0.293	0.778	0.297	0.815	0.622	0.817	0.661	0.937	0.559	0.921	0.538	0.829	0.687	0.964	0.924

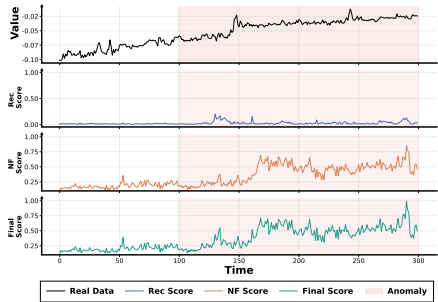


(a) Time steps 6500 to 8500 of the 7th variable in PSM

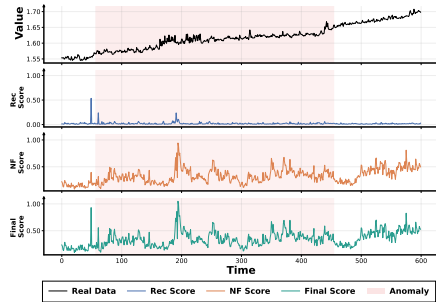


(b) Time steps 47700 to 49500 of the 13th variable in PSM

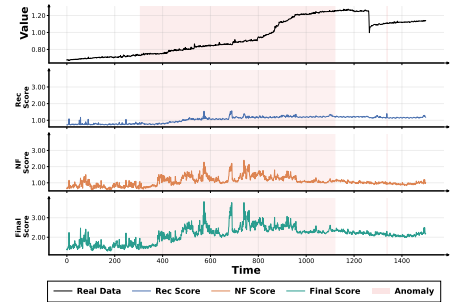
Fig. 6: Visualization of the effect of ADMM on the reconstruction performance of MAE in the PSM dataset.



(a) Time steps 7700 to 8000



(b) Time steps 47700 to 45300



(c) Time steps 5300 to 54500

Fig. 7: Visualization of the reconstruction score (Rec Score) and the anomaly score computed by normalizing flow (NF Score) for the 2nd variable in the PSM dataset.

suggests that the Masked Linear design is more suitable for multivariate density modeling, because its autoregressive structure with mask reversal allows inter-variable dependencies to be captured in a more structured way than fully connected layers.

H. Parameter Sensitivity Analysis

We also investigate the parameter sensitivity of VAN-AD. Fig. 5a reports the performance under different input window sizes. The results show that VAN-AD remains relatively stable across different window sizes, without significant performance fluctuations. In our experiments, the window size is typically set to 100 or 196. We also examine the effect of λ , which balances the local anomaly score and the global anomaly score. As shown in Fig. 5b, the model is generally robust to λ , and good performance can be achieved when λ is set within the range of 0.01 to 0.1.

I. Visualization

1) *The Effect of ADMM:* Fig. 6 visualizes the reconstruction results of MAE with ADMM (w/ ADMM) and without ADMM (w/o ADMM). The red curve denotes the reconstruction without ADMM, while the green curve denotes the reconstruction with ADMM. It can be observed that, in anomalous segments, MAE with ADMM produces more pronounced reconstruction errors, which makes anomalies easier to distinguish.

2) *The Effect of NFM:* We further visualize the working mechanism of VAN-AD. Fig. 7 presents the anomaly detection results of VAN-AD on the PSM dataset. The reconstruction scores are shown in the second row, the normalizing flow scores are shown in the third row, and the final anomaly scores are shown in the fourth row. It can be observed that when an anomalous segment is particularly long, reconstruction within the current window alone may produce low reconstruction scores, making it difficult to identify anomalies based only on reconstruction error. In contrast, NFM provides an additional

TABLE VIII: Base density experiments for VAN-AD. Fix denotes the use of a fixed base density, i.e., $p_Z(z_t) = \mathcal{N}(z_t | 0, I)$, whereas Rand denotes the use of a randomly initialized base density, corresponding to our default setting $p_Z(z_t) = \mathcal{N}(z_t | u, I)$.

Dataset	CalIt2		PSM		PUMP		SWAN	
	V-R	V-P	V-R	V-P	V-R	V-P	V-R	V-P
Fix	0.952	0.411	0.800	0.643	0.794	0.248	0.961	0.916
Rand	0.953	0.414	0.817	0.661	0.921	0.538	0.964	0.924

anomaly signal by estimating the probability density of the current window, thereby compensating for the limited local perception of MAE.

VI. CONCLUSION

In this paper, we investigate the transferability of pretrained large-scale vision models to time series anomaly detection, offering a new perspective beyond conventional Text-based and TS-based methods. By exploiting the structural similarity between images and time series, we propose VAN-AD, a novel framework that integrates masked autoencoder and normalizing flow for TSAD. To adapt MAE to this task, we design ADMM to alleviate the over-generalization issue in reconstruction, and develop NFM to model the global probability density of normal patterns, thereby addressing the limited local perception of MAE. Extensive experiments on multiple benchmark datasets demonstrate that VAN-AD consistently outperforms state-of-the-art methods across different evaluation metrics. We hope that this work can provide useful insights into cross-modal transfer for time series anomaly detection. In future work, we plan to: (1) explore other large-scale vision models for TSAD, for example, leveraging CLIP to perform contrastive learning on time series for anomaly detection; and (2) investigate more general and efficient time-series-to-image representations and adaptation mechanisms.

REFERENCES

- [1] A. Liang, Y. Sun, and N. Guizani, "Waverora: Wavelet rotary route attention for multivariate time series forecasting," *IEEE Transactions on Mobile Computing*, 2025.
- [2] Y. Yao, H. Jie, L. Chen, T. Li, Y. Gao, and S. Wen, "Tsec: An efficient and effective framework for time series classification," in *2024 IEEE 40th International Conference on Data Engineering (ICDE)*, pp. 1394–1406, IEEE, 2024.
- [3] H. Wang, Z. Chen, Z. Liu, L. Pan, H. Xu, Y. Liao, H. Li, and X. Liu, "Spot-i: Similarity preserved optimal transport for industrial iot data imputation," *IEEE Transactions on Industrial Informatics*, vol. 20, no. 12, pp. 14421–14429, 2024.
- [4] X. Wu, X. Qiu, Z. Li, Y. Wang, J. Hu, C. Guo, H. Xiong, and B. Yang, "Catch: Channel-aware multivariate time series anomaly detection via frequency patching," in *The Thirteenth International Conference on Learning Representations*.
- [5] B. Li, Q. Shentu, Y. Shu, H. Zhang, M. Li, N. Jin, B. Yang, and C. Guo, "Crossad: Time series anomaly detection with cross-scale associations and cross-window modeling," in *The Thirty-ninth Annual Conference on Neural Information Processing Systems*.
- [6] T. Yin, S. Fu, Z. Zhang, L. Huang, X. Zhang, Y. Yang, K. Yang, and M. Yan, "Scatterad: Temporal-topological scattering mechanism for time series anomaly detection," in *The Thirty-ninth Annual Conference on Neural Information Processing Systems*.
- [7] Q. Shentu, B. Li, K. Zhao, Y. Shu, Z. Rao, L. Pan, B. Yang, and C. Guo, "Towards a general time series anomaly detector with adaptive bottlenecks and dual adversarial decoders," in *13th International Conference on Learning Representations, ICLR 2025*, pp. 18810–18833, International Conference on Learning Representations, ICLR, 2025.
- [8] C. Liu, S. He, Q. Zhou, S. Li, and W. Meng, "Large language model guided knowledge distillation for time series anomaly detection," in *Proceedings of the Thirty-Third International Joint Conference on Artificial Intelligence*, pp. 2162–2170, 2024.
- [9] Z. Zhou and R. Yu, "Can llms understand time series anomalies?," in *The Thirteenth International Conference on Learning Representations*.
- [10] M. Chen, L. Shen, Z. Li, X. J. Wang, J. Sun, and C. Liu, "Visions: Visual masked autoencoders are free-lunch zero-shot time series forecasters," in *International Conference on Machine Learning*, pp. 8979–9007, PMLR, 2025.
- [11] L. Shen, M. Chen, X. Liu, H. Fu, X. Ren, J. Sun, Z. Li, and C. Liu, "Visions++: Cross-modal time series foundation model with continual pre-trained vision backbones," *arXiv preprint arXiv:2508.04379*, 2025.
- [12] Z. Li, S. Li, and X. Yan, "Time series as images: Vision transformer for irregularly sampled time series," *Advances in Neural Information Processing Systems*, vol. 36, pp. 49187–49204, 2023.
- [13] K. He, X. Chen, S. Xie, Y. Li, P. Dollár, and R. Girshick, "Masked autoencoders are scalable vision learners," in *Proceedings of the IEEE/CVF conference on computer vision and pattern recognition*, pp. 16000–16009, 2022.
- [14] K.-Y. Shen, "Learn hybrid prototypes for multivariate time series anomaly detection," in *The Thirteenth International Conference on Learning Representations*.
- [15] A. Vaswani, N. Shazeer, N. Parmar, J. Uszkoreit, L. Jones, A. N. Gomez, L. Kaiser, and I. Polosukhin, "Attention is all you need," *Advances in neural information processing systems*, vol. 30, 2017.
- [16] M. M. Breunig, H.-P. Kriegel, R. T. Ng, and J. Sander, "Lof: identifying density-based local outliers," in *Proceedings of the 2000 ACM SIGMOD international conference on Management of data*, pp. 93–104, 2000.
- [17] Z. He, X. Xu, and S. Deng, "Discovering cluster-based local outliers," *Pattern recognition letters*, vol. 24, no. 9-10, pp. 1641–1650, 2003.
- [18] M.-L. Shyu, S.-C. Chen, K. Sarinnapakorn, and L. Chang, "A novel anomaly detection scheme based on principal component classifier," 2003.
- [19] S. Ramaswamy, R. Rastogi, and K. Shim, "Efficient algorithms for mining outliers from large data sets," in *Proceedings of the 2000 ACM SIGMOD international conference on Management of data*, pp. 427–438, 2000.
- [20] A. Deng and B. Hooi, "Graph neural network-based anomaly detection in multivariate time series," in *Proceedings of the AAAI conference on artificial intelligence*, vol. 35, pp. 4027–4035, 2021.
- [21] Y. Xie, H. Zhang, and M. A. Babar, "Multivariate time series anomaly detection by capturing coarse-grained intra-and inter-variate dependencies," in *Proceedings of the ACM on Web Conference 2025*, pp. 697–705, 2025.
- [22] Y. Yang, C. Zhang, T. Zhou, Q. Wen, and L. Sun, "Dcdetector: Dual attention contrastive representation learning for time series anomaly detection," in *Proceedings of the 29th ACM SIGKDD conference on knowledge discovery and data mining*, pp. 3033–3045, 2023.
- [23] H. Kim, J. Mok, D. Lee, J. Lew, S. Kim, and S. Yoon, "Causality-aware contrastive learning for robust multivariate time-series anomaly detection," *arXiv preprint arXiv:2506.03964*, 2025.
- [24] S. Xiaoming, W. Shiyu, N. Yuqi, L. Dianqi, Y. Zhou, W. Qingsong, and M. Jin, "Time-moe: Billion-scale time series foundation models with mixture of experts," in *ICLR 2025: The Thirteenth International Conference on Learning Representations*, International Conference on Learning Representations, 2025.
- [25] A. F. Ansari, L. Stella, C. Turkmen, X. Zhang, P. Mercado, H. Shen, O. Shchur, S. S. Rangapuram, S. P. Arango, S. Kapoor, et al., "Chronos: Learning the language of time series," *Transactions on Machine Learning Research*, vol. 2024, 2024.
- [26] Y. Liu, H. Zhang, C. Li, X. Huang, J. Wang, and M. Long, "Timer: generative pre-trained transformers are large time series models," in *Proceedings of the 41st International Conference on Machine Learning*, pp. 32369–32399, 2024.
- [27] T. Zhou, P. Niu, L. Sun, R. Jin, et al., "One fits all: Power general time series analysis by pretrained lm," *Advances in neural information processing systems*, vol. 36, pp. 43322–43355, 2023.
- [28] Z. Zhang, H. Amiri, Z. Liu, L. Zhao, and A. Züfle, "Large language models for spatial trajectory patterns mining," in *Proceedings of the 1st ACM SIGSPATIAL International Workshop on Geospatial Anomaly Detection*, pp. 52–55, 2024.

- [29] M. Dong, H. Huang, and L. Cao, "Can llms serve as time series anomaly detectors?," *arXiv preprint arXiv:2408.03475*, 2024.
- [30] Y. Gong, Y.-A. Chung, and J. Glass, "Ast: Audio spectrogram transformer," *arXiv preprint arXiv:2104.01778*, 2021.
- [31] H. Touvron, M. Cord, M. Douze, F. Massa, A. Sablayrolles, and H. Jégou, "Training data-efficient image transformers & distillation through attention," in *International conference on machine learning*, pp. 10347–10357, PMLR, 2021.
- [32] J. Ni, Z. Zhao, C. A. Shen, H. Tong, D. Song, W. Cheng, D. Luo, and H. Chen, "Harnessing vision models for time series analysis: A survey," in *34th International Joint Conference on Artificial Intelligence, IJCAI 2025*, pp. 10612–10620, International Joint Conferences on Artificial Intelligence, 2025.
- [33] Z. Zhao, C. Shen, H. Tong, D. Song, Z. Deng, Q. Wen, and J. Ni, "From images to signals: Are large vision models useful for time series analysis?," *arXiv preprint arXiv:2505.24030*, 2025.
- [34] J. Deng, W. Dong, R. Socher, L.-J. Li, K. Li, and L. Fei-Fei, "Imagenet: A large-scale hierarchical image database," in *2009 IEEE conference on computer vision and pattern recognition*, pp. 248–255, Ieee, 2009.
- [35] E. Dai and J. Chen, "Graph-augmented normalizing flows for anomaly detection of multiple time series," in *International Conference on Learning Representations*, 2022.
- [36] Q. Zhou, S. He, H. Liu, J. Chen, and W. Meng, "Label-free multivariate time series anomaly detection," *IEEE Transactions on Knowledge and Data Engineering*, vol. 36, no. 7, pp. 3166–3179, 2024.
- [37] G. Papamakarios, T. Pavlakou, and I. Murray, "Masked autoregressive flow for density estimation," *Advances in neural information processing systems*, vol. 30, 2017.
- [38] P. Liu, H. Guo, T. Dai, N. Li, J. Bao, X. Ren, Y. Jiang, and S.-T. Xia, "Calf: Aligning llms for time series forecasting via cross-modal fine-tuning," in *Proceedings of the AAAI Conference on Artificial Intelligence*, vol. 39, pp. 18915–18923, 2025.
- [39] Y. Liu, T. Hu, H. Zhang, H. Wu, S. Wang, L. Ma, and M. Long, "itransformer: Inverted transformers are effective for time series forecasting," in *The Twelfth International Conference on Learning Representations*.
- [40] D. Luo and X. Wang, "Modernrntcn: A modern pure convolution structure for general time series analysis.,"
- [41] Y. Nam, S. Yoon, Y. Shin, M. Bae, H. Song, J.-G. Lee, and B. S. Lee, "Breaking the time-frequency granularity discrepancy in time-series anomaly detection," in *Proceedings of the ACM Web Conference 2024*, pp. 4204–4215, 2024.
- [42] Z. Zhuang, Y. Zhang, K. Zhao, C. Guo, B. Yang, Q. Wen, and L. Fan, "Noise matters: Cross contrastive learning for flink anomaly detection," *Proceedings of the VLDB Endowment*, vol. 18, no. 4, pp. 1159–1168, 2024.
- [43] C. Wang, Z. Zhuang, Q. Qi, J. Wang, X. Wang, H. Sun, and J. Liao, "Drift doesn't matter: Dynamic decomposition with diffusion reconstruction for unstable multivariate time series anomaly detection," in *Thirty-seventh Conference on Neural Information Processing Systems*, 2023.
- [44] A. Huet, J. M. Navarro, and D. Rossi, "Local evaluation of time series anomaly detection algorithms," in *Proceedings of the 28th ACM SIGKDD Conference on Knowledge Discovery and Data Mining*, pp. 635–645, 2022.
- [45] Q. Liu and J. Paparrizos, "The elephant in the room: Towards a reliable time-series anomaly detection benchmark," *Advances in Neural Information Processing Systems*, vol. 37, pp. 108231–108261, 2024.
- [46] X. Qiu, Z. Li, W. Qiu, S. Hu, L. Zhou, X. Wu, Z. Li, C. Guo, A. Zhou, Z. Sheng, J. Hu, C. S. Jensen, and B. Yang, "TAB: Unified benchmarking of time series anomaly detection methods," in *Proc. VLDB Endow.*, 2025.